Journal of the European Ceramic Society 37 (2017) 1509-1516.

DOI: 10.1016/j.jeurceramsoc.2016.12.014

http://dx.doi.org/10.1016/j.jeurceramsoc.2016.12.014

Investigations of $BaFe_{0.5}Nb_{0.5}O_3$ nano powders prepared by a low temperature aqueous synthesis and resulting ceramics

Roberto Köferstein* and Stefan G. Ebbinghaus

Institute of Chemistry, Martin Luther University Halle-Wittenberg,

Kurt-Mothes-Strasse 2, 06120 Halle, Germany.

* Corresponding author. Tel.: +49-345-5525630; Fax: +49-345-5527028.

E-mail address: roberto.koeferstein@chemie.uni-halle.de

Abstract. A facile method to prepare nanoscaled $BaFe_{0.5}Nb_{0.5}O_3$ via synthesis in boiling NaOH solution is described herein. The nano-crystalline powder has a high specific surface area of 55 $m^2\ g^{-1}$ and a crystallite size of 15 nm. The as-prepared powder does not show any significant crystallite growth up to 700 °C. The activation energy of the crystallite growth process was calculated as 590 kJ mol^{-1}. Dense ceramics can be obtained either after sintering at 1200 °C for 1 h or after two-step sintering at 1000 °C for 10 h. The average grain sizes of ceramic bodies can be tuned between 0.23 µm and 12 µm. The thermal expansion coefficient was determined as $11.4(3)\cdot10^{-6}\ K^{-1}$. The optical band gap varies between 2.90(5) and 2.63(3) eV. Magnetic measurements gave a Néel temperature of 20 K. Depending on the sintering regime, the ceramic samples reach permittivity values between 2800 and 137000 at RT and 1 kHz.

Investigations of $BaFe_{0.5}Nb_{0.5}O_3$ nano powders prepared by a low temperature aqueous synthesis and resulting ceramics

Roberto Köferstein* and Stefan G. Ebbinghaus

Institute of Chemistry, Martin Luther University Halle-Wittenberg,

Kurt-Mothes-Strasse 2, 06120 Halle, Germany.

* Corresponding author. Tel.: +49-345-5525630; Fax: +49-345-5527028.
E-mail address: roberto.koeferstein@chemie.uni-halle.de

Abstract. A facile method to prepare nanoscaled $BaFe_{0.5}Nb_{0.5}O_3$ via synthesis in boiling NaOH solution is described herein. The nano-crystalline powder has a high specific surface area of 55 $m^2\ g^{-1}$ and a crystallite size of 15 nm. The as-prepared powder does not show any significant crystallite growth up to 700 °C. The activation energy of the crystallite growth process was calculated as 590 kJ mol^{-1}. Dense ceramics can be obtained either after sintering at 1200 °C for 1 h or after two-step sintering at 1000 °C for 10 h. The average grain sizes of ceramic bodies can be tuned between 0.23 μm and 12 μm. The thermal expansion coefficient was determined as $11.4(3)\cdot10^{-6}\ K^{-1}$. The optical band gap varies between 2.90(5) and 2.63(3) eV. Magnetic measurements gave a Néel temperature of 20 K. Depending on the sintering regime, the ceramic samples reach permittivity values between 2800 and 137000 at RT and 1 kHz.

Keywords: *perovskites; barium iron niobate; ceramics, magnetism, permittivity, nano-particles*

1. Introduction

Perovskite materials with high relative permittivities (dielectric constants) are of interest because of their potential applications in advanced technology e.g. as memory devices, sensors, and capacitors [1,2,3,4]. Many of the corresponding materials, such as $Pb(Ti,Zr)O_3$ contain lead, therefore it is of importance to examine more eco-friendly materials like $BaFe_{0.5}Nb_{0.5}O_3$ that shows high dielectric constants over a wide temperature and frequency range with dielectric relaxation [5]. Patel et al. [6] reported that grain boundary effects are causal for the high permittivity values, whereas investigations by Wang et al. [7] suggest an oxygen defect induced dielectric behaviour. A possible ferroelectric nature of $BaFe_{0.5}Nb_{0.5}O_3$ is discussed controversially. Several authors suggest that $BaFe_{0.5}Nb_{0.5}O_3$ is a relaxor ferroelectric material [8,9,10,11,12,13], whereas other investigations show that $BaFe_{0.5}Nb_{0.5}O_3$ is a non-ferroelectric [6,7,14,15,16,17]. Additionally, structural investigations by Tezuka et al. [18], Galasso and Darby [19] as well as Bhagat and Prasad [20] point to a non-ferroelectric characteristic. In addition to its dielectric properties, $BaFe_{0.5}Nb_{0.5}O_3$ is an antiferromagnet with a Néel temperature of about 25 K [18] and also shows interesting catalytic activities. Voorhoeve et al. [21] used $BaFe_{0.5}Nb_{0.5}O_3$ for both the catalytic reduction of NO and the oxidation of CO. Recently, Pan et al. [22] and Chung et al. [23] reported on the dry reforming of methane with CO_2 to form syngas in the presence of $BaFe_{0.5}Nb_{0.5}O_3$. Usually $BaFe_{0.5}Nb_{0.5}O_3$ is synthesized by the conventional mixed-oxide method leading to coarse-grained powders [13,15,17,18,24,25,26,27]. In addition, fine-grained powders for ceramics with small and tuneable grain sizes have been prepared. For this purpose, several wet-chemical syntheses have been reported, such as sol-gel and co-precipitate routes [6,12,28]. A microwave assisted synthesis was developed by Charoenthai et al. [29]. A nanoscaled

$BaFe_{0.5}Nb_{0.5}O_3$ powder via a biosynthesis using Lactobacillus was reported by Jha et al. [30], which surprisingly showed a ferromagnetic behaviour.

The aim of this paper is to describe a fast and facile synthesis route for obtaining nanoscaled $BaFe_{0.5}Nb_{0.5}O_3$ with a high specific surface area. The reaction was carried out in boiling aqueous NaOH solution and the influence of the NaOH concentration on the particle growth kinetic was investigated. Furthermore, the sintering behaviour, phase evolution and microstructure of resulting ceramic bodies have been studied. Magnetic and dielectric measurements were carried out on samples obtained from different sintering regimes and the thermal expansion coefficient and the optical band gap were determined with respect to the particle size.

2. Experimental

2.1. Material preparation

$BaFe_{0.5}Nb_{0.5}O_3$ samples were prepared by reaction of Ba^{2+}-, Fe^{3+}-, and Nb^{5+}-reactants in boiling NaOH solutions with different concentrations. The reactions were carried out in PFA (perfluoroalkoxycoplomyer) round bottom flasks under argon atmosphere to avoid the formation of carbonates and silicon contaminations from glass.

$NbCl_5$ (0.01 mol, Alfa Aesar) was dissolved in 15 ml 2-methoxyethanol yielding a clear solution. In a separate solution $FeCl_3$ (0.01 mol, Alfa Aesar) and $BaCl_2 \cdot 2H_2O$ (0.02 mol, Fluka) were dissolved in 20 ml deionized water. 150 ml of an 8 M NaOH solution was heated up to about 70 °C and both the Nb- and the Fe/Ba-solutions were added slowly. The unified solution was refluxed for 5 h under vigorous stirring. Afterwards the resulting orange-ochre precipitate was filtered, washed with deionized water several times until no chloride ions were detectable and the pH value of the filtrate was about 7. The washed powder was dried at 120 °C for 2 h in air.

The synthesis was also carried out in 2 M, 6 M, 10 M, and 14 M NaOH solutions. The resulting as-prepared powders are donated as BFN-2M, BFN-6M, BFN-8M, BFN-10M, and BFN-14M in the following.

To obtain ceramic bodies, the as-prepared powder BFN-8M was mixed with 5 wt% of a saturated aqueous polyvinyl alcohol (PVA) solution as pressing aid and was uniaxially pressed (50 MPa) into pellets (green density 2.6 g cm^{-3}). These pellets were placed on a ZrO_2 fibre mat and sintered under conditions specified below.

2.2. Characterization

X-ray powder diffraction patterns were collected at room temperature on a *Bruker D8-Advance* diffractometer, equipped with a one-dimensional silicon strip detector (LynxEye™) and operating with Cu-K_α radiation. A counting time of 1s per data point and a step size of 0.01° were used. Crystallite size and the strain parameter were determined from the XRD line broadening (integral peak breadth) using the Scherrer and Wilson equation (software suite WinXPOW [31]). Dilatometric investigations were performed in flowing synthetic air (50 ml min^{-1}) in a *Setaram* TMA 92-16.18 dilatometer. Scanning electron microscope images were recorded with a *Phenom* ProX SEM in backscattered electron mode (BSE). TEM images were recorded with a *FEI* Titan 80-300 using an acceleration voltage of 300 kV. For magnetic measurements a *Quantum Design* PPMS 9 was used. Hysteresis loops were obtained with magnetic field cycling between –90 and +90 kOe. In addition, the temperature dependent magnetic moments were measured in the temperature range of 3–300 K under field-cooled (FC) and zero-field-cooled (ZFC) conditions. An Impedance Analyzer 4192A (*Hewlett Packard*) was used for permittivity measurements up to 10 MHz. Gold electrodes were sputtered onto the ceramic bodies in a *Cressington* Sputter Coater 108auto. Diffuse

reflectance spectra were recorded at room temperature using a *Perkin Elmer* UV–Vis spectrometer Lambda 19. $BaSO_4$ was used as white standard.

3. Results and discussion

3.1. Synthesis and powder characterization

The reactions were carried out in boiling NaOH solutions with various molarities (2, 6, 8, 10, and 14 M). The patterns of the as-prepared powders show reflections of $BaFe_{0.5}Nb_{0.5}O_3$ and traces of $BaCO_3$ (Fig. S1, Supporting information). The volume-weighted average crystallite sizes (size of a coherent scattering domain) of the as-prepared powders are 15–17 nm and do not differ significantly between the various samples. Additionally, the specific surface areas of the as-prepared powders are larger than 50 $m^2\ g^{-1}$ and do not vary significantly. Therefore, the NaOH concentration during the synthesis process has no significant influence on neither the crystallite size nor the specific surface area of the as-prepared powders (as illustrated in Fig. 1). However, an increasing NaOH concentration causes an increase of the strain parameter as seen from graph b in Fig. 1. After calcination of the as-prepared powders at 1000 °C for 2 h the XRD patterns show only reflections of the perovskite phase (Fig. S1, Supporting information). Only the samples prepared with 2 M and 6 M NaOH solution show a weak peak at $2\theta \approx 34°$ from traces of $BaFe_{12}O_{19}$. The crystallite size from the XRD line broadening after heating at 1000 °C rises with increasing NaOH concentration and accounts to 29 nm for sample BFN-2M and increases to 108 nm for BFN-14M (Fig. 1, Graph d). The reason for the increasing crystallite sizes most likely lies in the increase of the strain parameter in the as-prepared powders with rising NaOH concentration. The strain parameter reflects the amount of crystal lattice defects, which promote particle growth. As a conclusion a NaOH concentration less than 8 mol l^{-1} results in samples with trace impurities after calcination at 1000 °C, while a NaOH concentration above 8 mol l^{-1} leads to phase pure

samples with a considerable increase of the particle size after thermal treatment, caused by the larger amounts of lattice defects in the as-prepared powders.

To obtain phase pure samples with a reduced particle growth during thermal treatment we use the as-prepared powder BFN-8M for further investigations. The as-prepared powder BFN-8M has a specific surface area of 54.8 $m^2 g^{-1}$, corresponding to an equivalent particle size of 17 nm. The volume-weighted average crystallite size was calculated to be 15 nm and the root-mean-square strain was found to be $1.7 \cdot 10^{-3}$ from the XRD line broadening. TEM images show spherical particles in the range between 9 and 25 nm as seen from Fig. 2. XRD patterns of the powder BFN-8M after thermal treatment at various temperatures for 2 h is shown in Fig. 3. The small amount of $BaCO_3$ disappears after calcination above 800 °C and the peak widths decrease with rising temperature.

Fig. 4 shows the evolution of the crystallite size depending on the thermal treatment. Above 700 °C the crystallite size increases with rising temperature up to 57 nm, whereas the strain parameter decreases to $0.24 \cdot 10^{-3}$ at 1100 °C. Remarkably, we do not observe any significant crystallite growth up to 700 °C.

The kinetics of crystallite growth of powder BFN-8M during the thermal treatment between 800 and 1100 °C can be described by the following phenomenological equation (1) [32]:

$$D^n - D_0{}^n = kt \cdot e^{\frac{-E_A}{RT}} \qquad (1)$$

where D_0 is the initial crystallite size (15 nm), D the crystallite size after heating for the time t at temperature T, k is a pre–exponential constant, n the crystallite growth exponent, E_A the activation energy for the crystallite growth process and R the universal gas constant. The crystallite growth exponent n can be calculated from a plot of $D^n – D_0{}^n$ vs. t. For this purpose the crystallite sizes of sample BFN-8M after heat treatment at 900 °C for various times from 2 h up to 100 h were determined. The best fit to a straight line was calculated for n = 13.0 (Fig. 5a). Such high crystallite growth exponents are often found in nano- and submicro-sized

samples [33,34]. From the slope of an *Arrhenius* plot ($\ln((D^{13.0}-D_0^{13.0})/t)$ *vs.* T^{-1}) the activation energy of the crystallite growth process was calculated as E_A = 590±120 kJ mol^{-1} (Fig. 5b). The activation energy is higher than found for other nano-sizes oxide materials [33,35,36,37,38] and reflects the fact that the crystallite growth process starts only at high temperatures.

3.2. Sintering behaviour and microstructure of ceramic bodies

Fig. 6 shows the non-isothermal dilatometric measurement up to 1500 °C in flowing air of a compact from powder BFN-8M. The shrinkage process starts at about 710 °C, i.e. at the temperature at which the crystallite growth sets in, and the shrinkage rate achieves a maximum at 1035 °C with a value of -0.72 % min^{-1}. A second shrinkage maximum appears at 1266 °C (-0.23 % min^{-1}). The observed shrinkage rates are larger than 10^{-1} % min^{-1} indicate that the densification process is dominated by viscous flow [39]. The non-isothermal shrinkage process is finished at 1400 °C.

Fig. 7 shows the final bulk densities of ceramic bodies of BFN-8M after isothermal conventional sintering at various temperatures in static air (heating up with 5 K min^{-1}, soaking at this temperature for 1 h, cooling down with 5 K min^{-1}). The absolute bulk densities of the ceramics were determined from their weight and geometric dimensions. The relative bulk densities were calculated with respect to the single crystal density of 6.46 g cm^{-3} [19]. It turned out that dense ceramic bodies (relative density ≥ 90 %) can be obtained after one hour sintering at 1200 °C (5.94 g cm^{-3}). Upon rising the sintering temperature to 1250 °C the relative density reaches 96 % (6.18 g cm^{-3}). Higher sintering temperatures lead only to a marginal increase in density to 97 % (6.24 g cm^{-3}). The ceramic bodies show a significantly enhanced densification compared to the classical mixed-oxide method. Ceramics made from

powders prepared by this classical approach were reported to achieve relative densities above 90 % only for sintering times of 4 h at 1300 °C [10,40].

SEM images of selected ceramic bodies are depicted in Fig. 8 and derived grain sizes are summarized in Tab. 1. The average grain size ($\varnothing_{li}$) was determined by the lineal intercept method [41]. Sintering at 1100 °C results in small grains between 0.12 and 0.3 µm ($\varnothing_{li}$ = 0.23 µm), which slightly increase to 0.4–1.5 µm ($\varnothing_{li}$ = 1 µm) for T_s = 1200 °C. After sintering at 1400 °C the ceramic bodies consist of grains between 3 and 19 µm ($\varnothing_{li}$ = 11.7 µm).

To improve the densification behaviour we used a two-step sintering process [42,43]. In this approach, the compacts were first heated rapidly (20 K min^{-1}) to 1250 °C (T_1), then fast cooled (20 K min^{-1}) to a lower temperature of 1000 °C (T_2) and held at T_2 for 10 h (see inset in Fig. 8). This sintering procedure leads to ceramic bodies with a relative bulk density of 92 % (5.93 g cm^{-3}), grains between 0.20 and 1.20 µm, and an average grain size of 0.68 µm.

The average linear thermal expansion coefficient (α_{dil}) of bulk ceramics was determined by dilatometric measurements using equation 2 [44,45]:

$$\alpha_{dil} = \frac{\Delta L}{L_0 \Delta T} \qquad (2)$$

(L_0 – lengths of the ceramic body at RT, ΔL – length change in the temperature range ΔT). Measurements up to 600 °C reveal an average linear thermal expansion coefficient of 11.4(3)·10^{-6} K^{-1} which is close to the value found for $SrFe_{0.5}Nb_{0.5}O_3$ [46].

3.3 Diffuse reflectance, magnetic, and dielectric investigations

Diffuse reflectance spectra of BFN-8M ceramics after various sintering temperatures are shown for selected samples in Fig. 9. The *Kubelka–Munk* approach was used for analysis of the diffuse reflectance spectra as given by equation 3 [47,48]:

$$F(R) = \frac{\alpha}{s} = \frac{(1-R)^2}{2R} \qquad (3)$$

where $F(R)$ is the *Kubelka–Munk* function, R the reflectance, α the absorption coefficient and s is the scattering factor. Since the scattering factor is wavelength independent, $F(R)$ is proportional α [48]. The optical band gap can be determined according to equation 4 [49,50]:

$$\alpha h\nu = k(h\nu - E_g)^{1/n} \qquad (4)$$

where k is an energy-independent constant, E_g the optical band gap and the exponent n is determined by the type of transition. Using the *McLean* analysis [51,52] the optical band gap can be best described by a direct allowed transition (n = 2) in accordance with *Patel* at al. [53]. Thus, the optical band gap (E_g) can be determined by plotting $(F(R)\cdot h\nu)^2$ vs. $h\nu$ and extrapolating the slope to $F(R) \rightarrow 0$ (inset in Fig. 9). The as-prepared powder BFN-8M has an orange-ochre colour, which change to brown after treatment above 200 °C and at 1150 °C the samples show a dark-brown colour. The optical band gap for the as-prepared powder BFN-8M is 2.90(5) eV. After sintering at 1000 °C the band gap of the ceramics is reduced to 2.77(2) eV, decreases slightly to 2.63(3) eV for T_s = 1200 °C and does not change significantly up to T_s = 1400 °C (Fig. 10). The soaking time during the sintering process has no influence on the optical band gap. The two-step sintered ceramic (T_2 = 1000 °C) possesses an optical band gap of 2.65(2) eV.

Temperature dependent magnetization measurements of the as-prepared nano powder BFN-8M reveal that both the zero-field cooled (ZFC) and field cooled (FC) curves possess a Curie-Weiss behaviour. Below 10 K a separation between the FC and ZFC curves can be seen (Fig. 11) and the ZFC curve shows a weak maxima between 4–5 K. Fitting the high temperature data (50–300 K) to a Curie-Weiss law the magnetic moment per Fe^{3+} cation is calculated to

4.12 μ_B, which is smaller than the expected spin-only value of 5.92 μ_B for a high-spin configuration. Similar results were reported by Battle et al. [27] and they explained this finding by an extensive short-range ordering of the spins and the formation of spin clusters. A field-dependent measurement at 300 K reveals a linear correlation between the applied field and the magnetization indicating a paramagnetic behaviour (inset in Fig. 11). The temperature dependent magnetization behaviour of the as-prepared powder BFN-8M differs from the reported one for sintered bulk $BaFe_{0.5}Nb_{0.5}O_3$. Such samples show an antiferromagnetic behaviour with a Néel temperature (T_N) of ca. 25 K indicated by a maximum in the ZFC curve [9,18,24,27,54]. We suppose that the shift of the ZFC maximum in the nano BFN-8M powder is most likely a size effect. It was reported that a reduced particle size leads to a reduction of the Néel temperature [55,56]. Additionally, the as-prepared powder BFN-8M contains a large amounts of lattice defects, e.g. because of the incorporation of hydroxyl groups into the lattice, which is commonly found for syntheses in alkaline solutions [57,58]. Such lattice defects decrease after heat treatment. We observe that the formation of a distinct maximum (T_N) of the ZFC curve can be only obtained after sintering of BFN-8M (see below). The ZFC and FC curves of a ceramic body conventionally sintered at 1350 °C for 1 h are depicted in Fig. 12 and show the typical behaviour of $BaFe_{0.5}Nb_{0.5}O_3$ [18]. All ceramic samples have a Néel temperature of about 19–20 K, indicated by a maximum of the ZFC curve, which is about 5 K lower than for samples prepared by the conventional mixed-oxide method [27]. The Néel temperature of our samples was found to be independent on the sintering procedure and grain-size. The paramagnetic region above 20 K does not show a Curie-Weiss behaviour, because of a ferromagnetic contribution as seen in the inset of Fig. 12. This field-dependent measurement at 300 K reveals a linear increase of the magnetization and the appearance of a hysteresis loop that indicates the presence of a weak spontaneous magnetization. The corresponding saturation magnetization at 300 K (M_s) of this ferro-/ferrimagnetic contribution lies in the range of 0.72 – 0.78 emu g^{-1}. The M_s values were

calculated by a linear extrapolation of the magnetization at highest field to H = 0. The coercivity values decrease with raising sintering temperature from H_c = 5.5 kOe (1100 °C) to 0.6 kOe (1400 °C) primarily caused by increasing grain sizes [59,60]. The weak spontaneous magnetization is most probably caused by trace impurities of $BaFe_{12}O_{19}$ as a ferrimagnetic second phase. In fact, XRD measurements (Fig. 13) with 10 s counting time per data point reveal very weak reflections of $BaFe_{12}O_{19}$. Reported saturation magnetization values for polycrystalline $BaFe_{12}O_{19}$ are between 57 and 66 emu g^{-1} at room temperature [61,62]. Based on these values, the amount of $BaFe_{12}O_{19}$ in the ceramic samples can be estimated to be 1.1–1.4 wt%. Sintering with longer soaking time leads to a considerable reduction of the spontaneous magnetization, e.g. from 0.76 emu g^{-1} to 0.07 emu g^{-1} after sintering at 1350 °C for 1 h and 50 h (inset in Fig. 12), respectively. In addition the very weak reflections of $BaFe_{12}O_{19}$ in the XRD pattern disappear (Fig. 13). It can be concluded that the reported very large magnetic moments and the appearance of ferromagnetism for some $BaFe_{0.5}Nb_{0.5}O_3$ samples [24,30] is caused by small amounts of secondary phases such as $BaFe_{12}O_{19}$, which have not been detected due to poor data quality of the corresponding XRD patterns.

Frequency dependent dielectric measurements at 22 °C between 0.1 kHz and 10 MHz for BFN-8M ceramics are shown in Fig. 14. All ceramics show a decrease in the relative permittivity (ε_r) with increasing frequency. The high values of ε_r in the low frequency region have been explained by Maxwell-Wagner interface polarisation [6,16,63,64]. At a frequency of 1 kHz permittivity values are between 2700 and 137000 with tan δ values ranging from 0.48 to 2.2 depending on the sintering regime. Between 0.1 kHz and 100 kHz the permittivity values decrease by 68 %, 80 %, and 92 % for ceramics sintered at 1150, 1350, and 1400 °C for 1 h, respectively. On the other hand, the ceramic body conventionally sintered at 1200 °C as well as the two-step sintered sample show only a reduction of 54 %, which is considerable lower than for $BaFe_{0.5}Nb_{0.5}O_3$ ceramic prepared by a sol-gel and an oxalate-based co-precipitation method [6,28]. At low frequencies the relative permittivities of the

conventionally sintered samples increase with rising sintering temperature due to larger grain sizes and increasing densities, which reduce pore-charging effects [65,66]. At frequencies above 1 MHz all samples show basically the same behaviour. For the loss tangent such a clear dependence on the sintering temperature was not found, but all samples show the same frequency trend, i.e. a linear decrease of tan δ in the range 0.1 to 10 kHz followed by increasing values with a maximum at about 4 MHz. The sample obtained by the two-step sintering process closely resembles the behaviour of the one conventionally sintered at 1200 °C, reflecting their identical densities. However, the grain size of the two-step sintered ceramics is smaller than the sample after sintering at 1200 °C.

The temperature dependent development of the relative permittivity and the dissipation factor between 25 °C and 200 °C at a frequency of 1 kHz are shown in Fig. 15. All samples show rising permittivity and tan δ values with temperature. Additionally the ceramics sintered at 1200 and 1350 °C exhibit a sigmoidal development, which was also found in other investigations of $BaFe_{0.5}Nb_{0.5}O_3$ [5,11,67,68]. The sample sintered at 1350 °C shows between 25 °C and about 100 °C only a slight increase of the permittivity from 48000 to 64000, which rises to 230000 at 200 °C. Considering the entire temperature range the sample sintered at 1200 °C shows the strongest temperature dependency of the permittivity, whereas the two-step sintered ceramic exhibit the lowest one. Moreover, the dissipation factor (tan δ) rises with temperature and the ceramic sintered at 1350 °C shows the lowest values.

Compared with $BaFe_{0.5}Nb_{0.5}O_3$ ceramics obtained by the mixed-oxide method [7,9,25,40,69] the soft-chemistry synthesis described herein leads to ceramics with up to one order of magnitude higher permittivity values, which additionally show a lower temperature dependency. The reason may be that ceramics prepared by the mixed-oxide method were sintered with longer soaking times leading to higher defect concentrations.

4. Conclusion

Nano-size $BaFe_{0.5}Nb_{0.5}O_3$ powders with a high specific surface area of about 55 $m^2\ g^{-1}$ and crystallite sizes of ca. 15 nm were synthesized by a low temperature aqueous syntheses in boiling NaOH. The concentration of the NaOH solution influences the crystallite growth of the as-prepared powders in a successive heating step in air. It was found that a molarity of 8 mol l^{-1} NaOH was optimal to obtain phase-pure samples with reduced particle growth during heat treatment. Non-isothermal dilatometric investigations of a compacted powder show that the shrinkage begins at 710 °C and is completed at 1400 °C. Ceramic samples with relative densities ≥ 90 % can be obtained after conventional sintering at 1200 °C for 1 h or by a two-step sintering procedure at 1000 °C for 10 h. The average grain sizes of ceramic bodies varied between 0.23 µm and 12 µm depending on the sintering regime. The average linear thermal expansion coefficient was calculated to be $11.4(3)\cdot10^{-6}$ K^{-1}. The ceramics show an antiferromagnetic behaviour with a Néel temperature of 19–20 K independent of the sintering regime. A found weak spontaneous magnetization above 20 K was found to be caused by small traces of $BaFe_{12}O_{19}$. Dielectric measurements were carried out depending on frequency and temperature. The obtained dielectric behaviour of the ceramic samples depends on the sintering regime. The ceramics show typical relaxor-type behaviour with increasing permittivity values at low frequencies. The ε_r and tan δ values increase with temperature. Sintering at 1350 °C leads to ceramics with the highest permittivity values combined with the lowest tan δ values. Moreover, ceramic obtained after a two-step sintering process shows the lowest temperature and frequency dependency of the permittivity. In contrast to other reports, our investigations did not show any evidence for ferroelectricity in $BaFe_{0.5}Nb_{0.5}O_3$.

In summary, the introduced synthesis route leads to nano powders with improved densification behaviour and in turn to ceramic bodies with tuneable grain sizes in a wide

range, which show superior dielectric properties compared to samples obtained by the mixed-oxide method.

Acknowledgements

We are grateful to Dr. E. Pippel (Max Planck Institute of Microstructure Physics, Halle/Saale) for TEM investigations. Financial support by the German Research Foundation within the Collaborative Research Centre (SFB 762) *Functionality of Oxide Interfaces* is gratefully acknowledged.

Appendix A. Supplementary data

Supplementary data associated with this article can be found, in the online version, at http://dx.doi.org/

References

[1] C.C. Homes, T. Vogt, S.M. Shapiro, S. Wakimoto, A.P. Ramirez, Optical response of

high-dielectric-constant perovskite-related oxide, *Science* 293 (2001) 673–676.

[2] S.Y. Chung, I.D. Kim, S.J. Kang, Strong nonlinear current–voltage behaviour in perovskite-derivative calcium copper titanate, *Nat. Mater.* 3 (2004) 774–778.

[3] G.H. Haertling, Ferroelectric Ceramics: History and Technology, *J. Am. Ceram. Soc.* 82 (1999) 797–818.

[4] R. Vivekanandan, T.R.N. Kutty, Grain boundary layer ceramic capacitors based on donor-doped $Ba(Ti_{1-x}Sn_x)O_3$. *Mater. Sci. Eng. B* 6 *(*1990) 221–31.

[5] S. Ke, H. Fan, H. Huang, Dielectric relaxation in A_2FeNbO_6 (A=Ba, Sr, and Ca) perovskite ceramics, *J. Electroceram.* 22 (2009) 252–256.

[6] P.K. Patel, K.L. Yadav, H. Singh, A.K. Yadav, Origin of giant dielectric constant and magnetodielectric study in $Ba(Fe_{0.5}Nb_{0.5})O_3$ nanoceramics *J. Alloys Compd.* 591 (2014) 224–229.

[7] Z. Wang, X.M. Chen, L. Ni, X.Q. Liu, Dielectric abnormities of complex perovskite $Ba(Fe_{1/2}Nb_{1/2})O_3$ ceramics over broad temperature and frequency range, *Appl. Phys. Lett.* 90 (2007) 022904.

[8] M. Ganguly, S. Parida, E. Sinha, S.K. Rout, A.K. Simanshu, A. Hussain, I.W. Kim, Structural, dielectric and electrical properties of $BaFe_{0.5}Nb_{0.5}O_3$ ceramic prepared by solid-state reaction technique, *Mater. Chem. Phys.* 131 (2011) 535–539.

[9] D. Bochenek, Z. Surowiak, J. Poltierova-Vejpravova, Producing the lead-free $BaFe_{0.5}Nb_{0.5}O_3$ ceramics with multiferroic properties, *J. Alloys Compd.* 487 (2009) 572–576.

[10] P. Kantha, N. Pisitpipathsin, K. Pengpat, S. Eitssayeam, G. Rujijanagul, R. Guo, A.S. Bhalla, Dielectric relaxation and electrical properties of lead-free perovskite $BaGe_x(Fe_{0.5}Nb_{0.5})_{1-x}O_3$ ceramic, *Ferroelectrics* 473 (2014) 1–12.

[11] S. Ke, H. Huang, H. Fan, H.L.W. Chan, L.M. Zhou, Colossal dielectric response in barium iron niobate ceramics obtained by different precursors, *Ceram. Int.* 34 (2008) 1059–1062.

[12] C.-Y. Chung, Y.-H. Chang, G.-J. Chen, Y.-L. Chai, Preparation, structure and ferroelectric properties of $Ba(Fe_{0.5}Nb_{0.5})O_3$ powders by sol–gel method, *J. Cryst. Growth* 284 (2005) 100–107.

[13] S. Saha and T.P. Sinha, Low-temperature scaling behavior of $BaFe_{0.5}Nb_{0.5}O_3$, *Phys. Rev. B* 65 (2002) 134103.

[14] I.P. Raevski, S.A. Prosandeev, A.S. Bogatin, M.A. Malitskaya, L. Jastrabik, High dielectric permittivity in $AFe_{1/2}B_{1/2}O_3$ nonferroelectric perovskite ceramics (A=Ba, Sr, Ca; B=Nb, Ta, Sb), J. *Appl. Phys.* 93 (2003) 4130–4136.

[15] I.P. Raevski, S.A. Kuropatkina, S.P. Kubrin, S.I. Raevskaya, V.V. Titov, D.A. Sarychev, M.A. Malitskaya, A.S. Bogatin, I.N. Zakharchenko, Dielectric and Mössbauer studies of high-permittivity $BaFe_{1/2}Nb_{1/2}O_3$ ceramics with cubic and monoclinic perovskite structures, *Ferroelectrics* 379 (2009) 48–54.

[16] S.K. Kar and P. Kumar, Structural, morphological and dielectric study of $Ba(FeNb)_{0.5}O_3$ ceramics synthesized by microwave processing technique, *J. Phys. Chem. Solids* 74 (2013) 1408–1413.

[17] S.K. Kar and P. Kumar, Permittivity and modulus spectroscopic study of $BaFe_{0.5}Nb_{0.5}O_3$ ceramics, *Process. Appl. Ceram*. 7 (2013) 181–187.

[18] K. Tezuka, K. Henmi, Y. Hinutsa, Magnetic susceptibilities and Mössbauer spectra of perovskites A_2FeNbO_6 (*A*=Sr, Ba), *J. Solid State Chem.* 154 (2000) 591–597.

[19] F. Galasso, W. Darby, Ordering of the octahedrally coördinated cation position in the perovskite structure, *J. Phys. Chem.* 66 (1962) 131–132.

[20] S. Bhagat and K. Prasad, Structural and impedance spectroscopy analysis of $Ba(Fe_{1/2}Nb_{1/2})O_3$ ceramic, *Phys. Status Solidi* A 207 (2010) 1232–1239.

[21] R.J.H. Voorhoeve, L.E. Trimble, C.P. Khattak, Exploration of perovskite-like catalysts: Ba_2CoWO_6 and Ba_2FeNbO_6 in NO reduction and CO oxidation, *Mater. Res. Bull.* 9 (1974) 655–666.

[22] W.-C. Chung, K.-L. Pan, H.-M. Lee, M.-B. Chang, Dry reforming of methane with dielectric barrier discharge and ferroelectric packed-bed reactors, *Energy Fuels* 28 (2014) 7621–7631.

[23] K.L. Pan, W.C. Chung, M.B. Chang, Dry reforming of CH_4 with CO_2 to generate syngas by combined plasma catalysis, *IEEE Trans. Plasma Sci.* 42 (2014) 3809–3818.

[24] N. Rama, J.B. Phillip, M. Opel, K. Chandrasekaran, V. Sankaranarayanan, R. Gross, M.S.R. Rao, Study of magnetic properties of $A_2B'NbO_6$ (A=Ba,Sr,BaSr; and B'=Fe and Mn) double perovskites, *J. Appl. Phys.* 95 (2004) 7528–7530.

[25] U. Intatha, S. Eitssayeam, T. Tunkasiri, Giant dielectric behaviour of $BaFe_{0.5}Nb_{0.5}O_3$ perovskite ceramic, *Int. J. Mod. Phys.* 22 (2008) 4717–4723.

[26] X.H. Sun, C.C. Wang, G.J. Wang, C.M. Lei, T. Li, J.Y. Mei, Y.M. Cui, Relationship between the dielectric properties and the conductivity of Ba_2FeNbO_6, *J. Electroceram.* 29 (2012) 187–191.

[27] P.D. Battle, T.C. Gibb, A.J. Herod, S.-H. Kim, P.H. Munns, Investigation of magnetic frustration in A_2FeMO_6 (A=Ca, Sr, Ba; M=Nb, Ta, Sb) by magnetometry and Mössbauer spectroscopy, *J. Mater. Chem.* 5 (1995) 865–870.

[28] Z. Wang, Y.F. Wen, H.J. Li, M.R. Fang, C. Wang, Y.P. Pu, Excellent stability and low dielectric loss of $Ba(Fe_{0.5}Nb_{0.5})O_3$ synthesized by a solution precipitation method, *J. Alloys Compd.* 656 (2016) 431–438.

[29] N. Charoenthai, R. Traiphol, G. Rujijanagul, Microwave synthesis of barium iron niobate and dielectric properties, *Mater. Lett.* 62 (2008) 4446–4448.

[30] A.K. Jha and K. Prasad, Green synthesis and characterization of $BaFe_{0.5}Nb_{0.5}O_3$ nanoparticles, *J. Chin. Adv. Mater. Soc.* 2 (2014) 294–302.

[31] Program WinXPOW v2.11, Stoe & Cie GmbH, Darmstadt, 2004.

[32] W. Cun, W. Xinming, Z. Jincai, M. Bixian, S. Guoying, P. Ping′an, F. Jiamo, Synthesis, characterization and photocatalytic property of nano-sized Zn_2SnO_4, *J. Mater. Sci.* 37 (2002) 2989–2996.

[33] A.M. Pourrahimi, D. Liu, V. Ström, M.S. Hedenqvist, R.T. Olsson, U.W. Gedde, Heat treatment of ZnO nanoparticles: new methods to achieve high-purity nanoparticles for high high-voltage applications *J. Mater. Chem.* A3 (2015) 17190–17200.

[34] R. Köferstein, T. Walther, D. Hesse, S.G. Ebbinghaus, Crystallite growth, phase transition, magnetic properties, and sintering behaviour of nano-$CuFe_2O_4$ powders prepared by a combustion-like process, *J. Solid State Chem.* 213 (2014) 57–64.

[35] M. Popa, J. Frantti, M. Kakihana, Lanthanum ferrite $LaFeO_{3+d}$ nanopowders obtained by the polymerizable complex method, *Solid State Ionics* 154–155 (2002) 437–445.

[36] R. Köferstein, T. Buttlar, S.G. Ebbinghaus, Investigations on $Bi_{25}FeO_{40}$ powders synthesized by hydrothermal and combustion-like processes, *J. Solid State Chem.* 217 (2014) 50–56.

[37] W. Cun, W. Xinming, Z. Jincai, M. Bixian, S. Guoying, P. Ping′An, F. Jiamo, Synthesis, characterization and photocatalytic property of nano-sized Zn_2SnO_4, *J. Mater. Sci.* 37 (2002) 2989–2996.

[38] Y. Kotera, T. Saito, M. Terada, Crystal growth of magnesium oxide prepared by the thermal decomposition of magnesium hydroxide, *Bull. Chem. Soc. Jpn.* 36 (1963) 195–199.

[39] W. Schatt, *Sintervorgänge*. VDI-Verlag, Düsseldorf, 1992, pp. 78–100.

[40] S. Eitssayeam, U. Inthata, K. Pengpatr, T. Tunkasiri, Preparation and characterization of barium iron niobate ($BaFe_{0.5}Nb_{0.5}O_3$) ceramics, *Curr. Appl. Phys.* 6 (2006) 316–318.

[41] M.I. Mendelson, Average grain size in polycrystalline ceramics, *J. Am. Ceram. Soc.* 52 (1969) 443–446.

[42] I.-W. Chen and X -H. Wang, Sintering dense nanocrystalline ceramics without final-stage grain growth, *Nature* 404 (2000) 168–171.

[43] R. Köferstein and S.G. Ebbinghaus, $BaGeO_3$ as sintering additive for $BaTiO_3$–$MgFe_2O_4$ composite ceramics, *RSC Adv.* 5 (2015) 71491–71499.

[44] J.D James, J.A Spittle, S.G.R Brown, R.W Evans, A review of measurement techniques for the thermal expansion coefficient of metals and alloys at elevated temperatures *Meas. Sci. Technol.* 12 (2001) R1–R15.

[45] W.F. Hemminger and H.K. Cammenga, *Methoden der Thermischen Analyse.* Springer-Verlag, Berlin-Heidelberg, 1989.

[46] T. Xia, X.D. Liu, Q. Li, J. Meng, X.Q. Cao, Synthesis, structural and electrical characterizations of $Sr_2Fe_{1-x}M_xNbO_6$ (M = Zn and Cu) with double perovskite structure, *J. Alloys Compd.* 422 (2006) 264–272.

[47] P. Kubelka and F. Munk, Ein Beitrag zur Optik der Farbanstriche, *Z. Techn. Phys.* 11 (1931) 593–601.

[48] G. Kortüm and J. Vogel, Die Theorie der diffusen Reflexion von Licht an pulverförmigen Stoffen, *Z. Phys. Chem.* 18 (1958) 110–122.

[49] M. Nowak, B. Kauch, P. Szperlich, Determination of energy band gap of nanocrystalline SbSI using diffuse reflectance spectroscopy, *Rev. Sci. Instrum.* 80 (2009) 046107.

[50] R. Lopez, R. Gomez, Band-gap energy estimation from diffuse reflectance measurements on sol–gel and commercial TiO_2: a comparative study *J. Sol-Gel Sci. Technol.* 61 (2012) 1–7.

[51] O. Schevciw and W.B. White, The optical absorption edge of rare earth sesquisulfides and alkaline earth – rare earth sulfides. *Mater. Res. Bull.* 18 (1983) 1059–1068.

[52] T.P McLean, in: Progress in Semiconductors, ed. A.F. Gibson, Heywood, London, 1960, Vol. 5, pp. 55–102.

[53] P.K. Patel, K.L. Yadav, G. Kaur, Reduced dielectric loss in $Ba_{0.95}Sr_{0.05}(Fe_{0.5}Nb_{0.5})O_3$ thin film grown by pulsed laser deposition, *RSC Adv.* 4 (2014) 28056–28061.

[54] I.O Troyanchuck, M.V. Bushinsky, A.N. Chobot, O.S. Mantytskaya, N.V. Pushkarev, R. Szymczak, Crystal-structure and magnetic phase transformations in solid solutions of $BiFeO_3$–$AFe_{0.5}Nb_{0.5}O_3$ (A = Ca, Sr, Ba, Pb), *J. Exp. Theor. Phys*. 107 (2008) 245–250.

[55] S. Shetty, V.R. Palkar, R. Pinto, Size effect study in magnetoelectric $BiFeO_3$ system, *Prama – J. Phys.* 58 (2002) 1027–1030.

[56] X.G. Zheng, C.N. Xu, K. Nishikubo, K. Nishiyama, W. Higemtot, W.J. Moon, E. Tanaka, E.S. Otabe, Finite-size effect on Néel temperature in antiferromagnetic nanoparticles, *Phys. Rev.* B72 (2005) 014464.

[57] G. Busca, V. Buscaglia, M. Leoni, P. Nanni, Solid-state and surface spectroscopic characterization of $BaTiO_3$ fine powders, *Chem. Mater.* 6 (1994) 955–961.

[58] D.F.K. Hennings, C. Metzmacher, B.S. Schreinemacher, Defect chemistry and microstructure of hydrothermal barium titanate, *J. Am. Ceram. Soc.* 894 (2001) 179–182.

[59] D.L. Huber, Synthesis, Properties, and Applications of Iron Nanoparticles *Small* 5 (2005) 482–501.

[60] J. Dho, E.K. Lee, J.Y. Park, N.H. Hur, Effects of the grain boundary on the coercivity of barium ferrite $BaFe_{12}O_{19}$, *J. Magnet. Magnet. Mater.* 285 (2005) 164–168.

[61] J. Yu, S. Tang, L. Zhai, Y. Shi, Y. Du, Synthesis and magnetic properties of single-crystalline $BaFe_{12}O_{19}$ nanoparticles, *Physica B* 404 (2009) 4253–4256.

[62] M.S.E. Shafie, M. Hashim, I. Ismail, S. Kanagesan, M.I. Fadzidah, I.R. Idza, A. Hajalilou, R. Sabbaghizadeh, Magnetic M–H loops family characteristics in the microstructure evolution of $BaFe_{12}O_{19}$, *J. Mater. Sci.: Mater. Electron.* 25 (2014) 3787–3794.

[63] N.K. Singh, P. Kumar, A.K. Sharma, R.N.P. Choudhary, Structural and electrical characteristics of $Ba(Fe_{0.5}Nb_{0.5})O_3$-$SrTiO_3$ ceramic system, *Mater. Sci. Appl.* 2 (2011) 1593–1600.

[64] K.W. Wagner, Erklärung der dielektrischen Nachwirkungsvorgänge auf Grund Maxwellscher Vorstellungen, *Arch. Elektrotech.* 2 (1914) 371–387.

[65] K. Okazaki and K. Nagata, Effects of grain size and porosity on electrical and optical properties of PLZT ceramics, *J. Am. Ceram. Soc.* 56 (1973) 82–86.

[66] C.-C. Hsueh, M.L. Mecartney, W.B. Harrison, M.R.B. Hanson, B.G. Koepke, Microstructure and electrical properties of fast-fired lead zirconate-titanate ceramics, *J. Mater. Sci. Lett.* 8 (1989) 1209–1216.

[67] U. Intatha, K. Sathitada, S. Eitssayeam, K. Pengpat, G. Rujijanagul, P. Thavornyuttakarn, T. Tunkasiri, Effects of potassium fluoride salt additive on the sintering temperature and dielectric properties of $BaFe_{0.5}Nb_{0.5}O_3$ ceramics. *Adv. Mater. Res.* 55–57 (2008) 885–888.

[68] D. Bochenek, P. Niemiec, I. Szafraniak-Wiza, M. Adamczyk, R. Skulski, Preparation and dielectric properties of the lead-free $BaFe_{1/2}Nb_{1/2}O_3$ ceramics obtained from mechanically triggered powder, *Eur. Phys. J.* B88 (2015) 277.

[69] P. Kantha, N. Pisitpipathsin, K. Pengpat, G. Rujijanagul, R. Guo, A.S. Bhalla, Microstructure and electrical properties of $BaFe_{0.5}Nb_{0.5}O_3$ doped with GeO_2 (1–5 wt.%), *Ferroelectrics* 425 (2011) 27–38.

Table 1

Overview of the ceramic bodies

Sintering regime	Average grain size [1] (Grain size range)	ε_r [4]	tan δ [4]
Conventional sintering [2]			
1100 °C, 1 h	0.23 μm (0.12–0.3 μm)		
1150 °C, 1 h	0.350 nm (0.16–0.5 μm)	2760	0.88
1200 °C, 1 h	1 μm (0.4–1.5 μm)	5940	0.48
1250 °C, 1 h	2.1 μm (0.7–4.1 μm)		
1350 °C, 1 h	8.7 μm (2.5–12 μm)	50710	0.48
1400 °C, 1 h	11.7 μm (3.0–19 μm)	137210	2.23
2-step sintering [3]			
T_1 = 1250 °C T_2 = 1000 °C, 10 h	0.68 μm (0.20–1.2 μm)	4830	0.50

1) Lineal intercept method; 2) Temperature rate 5 K min^{-1}; 3) Temperature rate 20 K min^{-1}; 4) 22 °C, 1 kHz

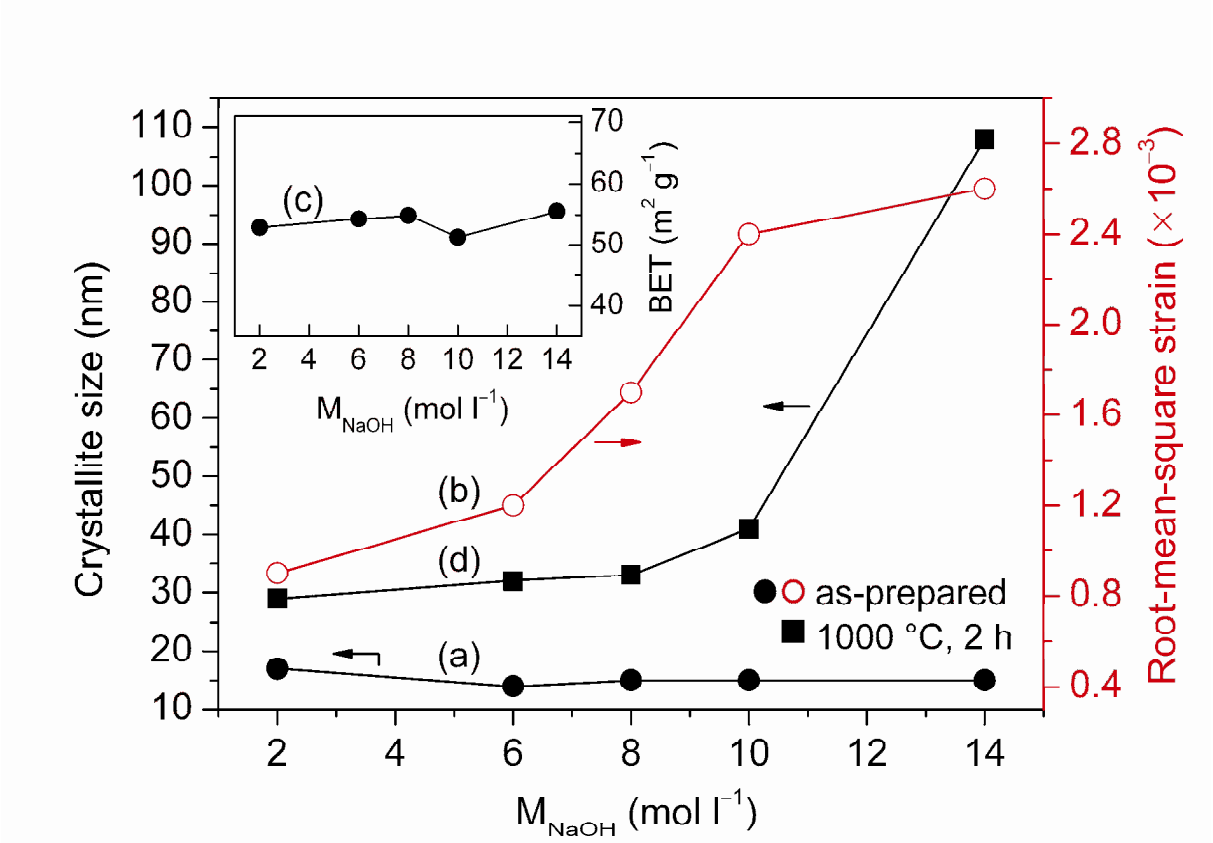

Fig. 1 Development of (a) volume-weighted average crystallite size, (b) root-mean-square strain, and (c) specific surface area of as-prepared powders depending on the initial NaOH concentration. Graph (d) shows the crystallite size of the powders after heating at 1000 °C for 2 h versus NaOH concentration.

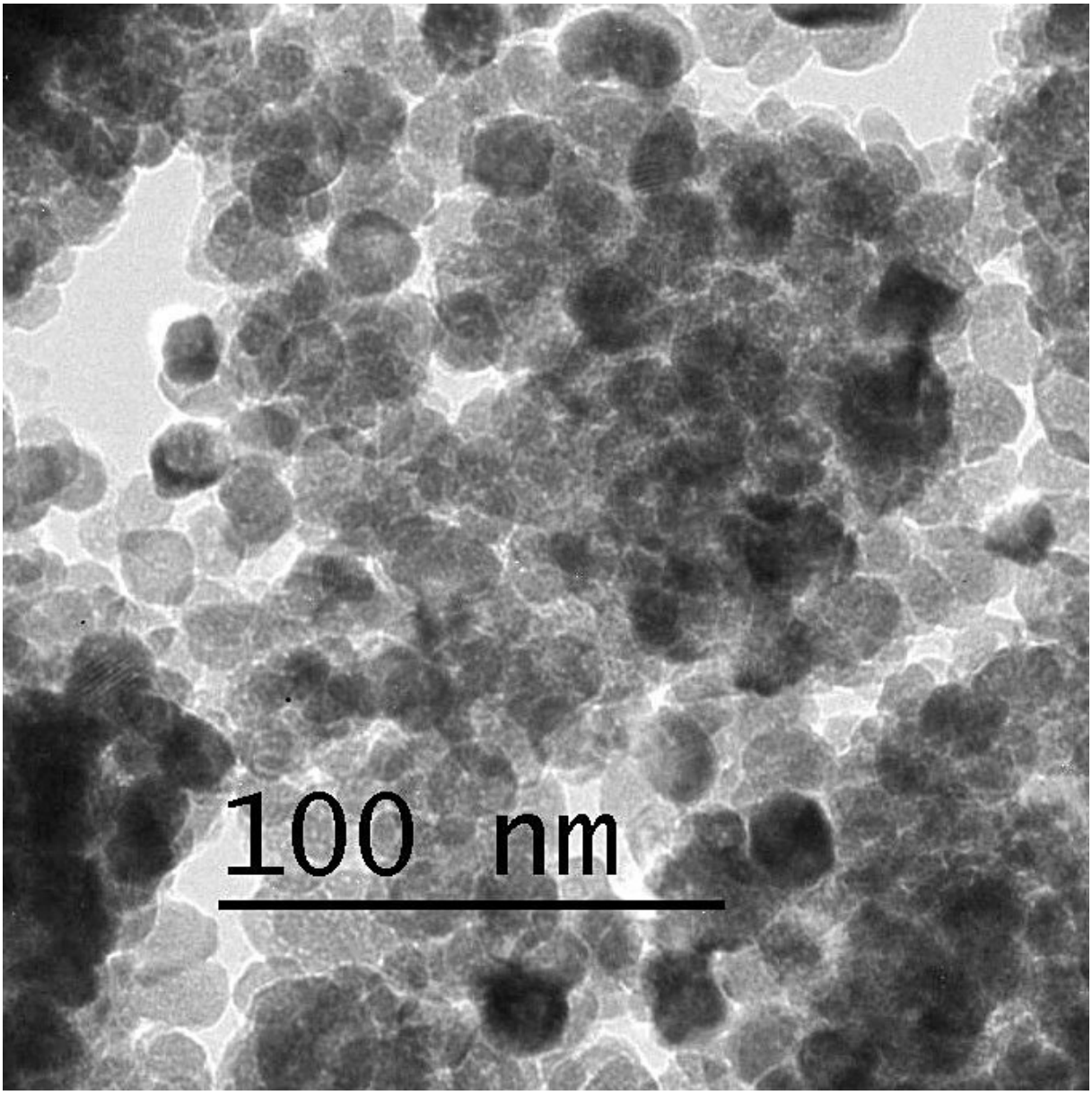

Fig. 2 TEM image of the as-prepared powder BFN-8M.

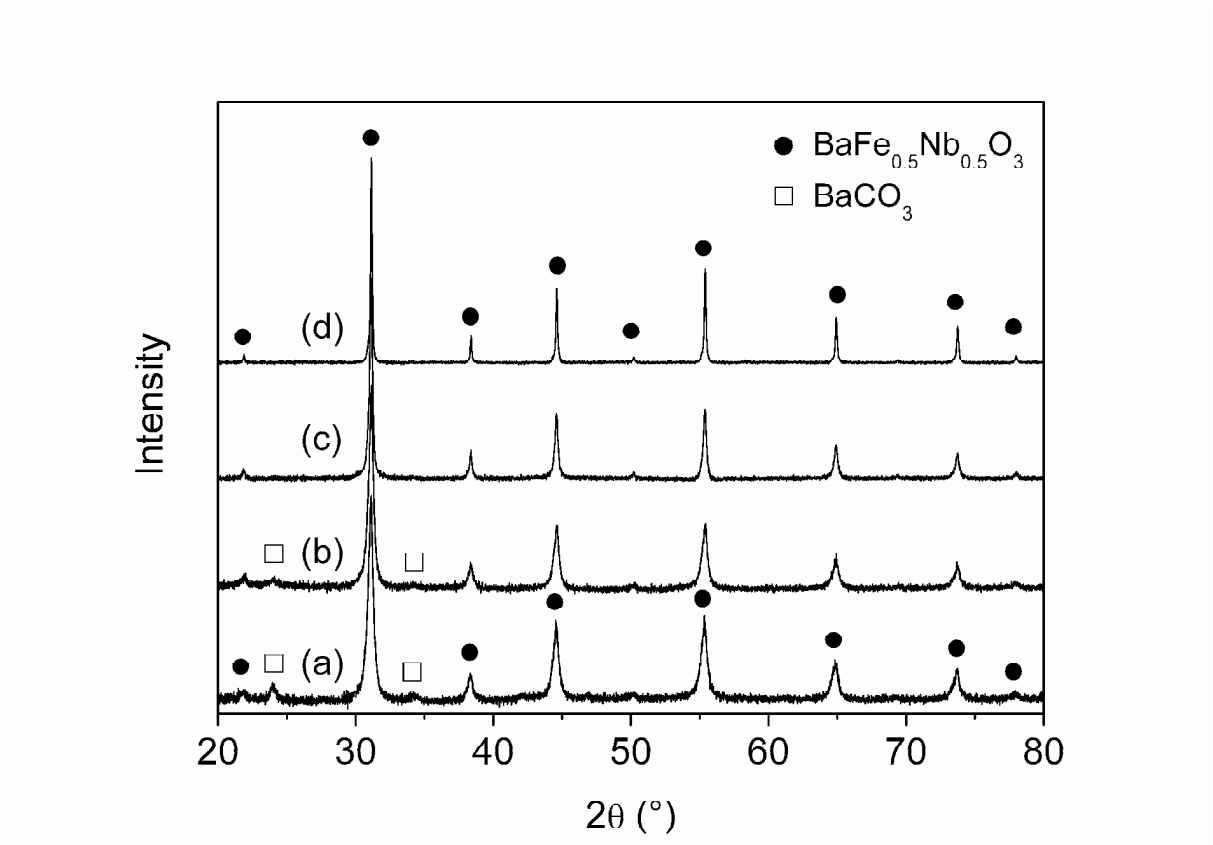

Fig. 3 XRD patterns of powder BFN-8M after heating at various temperatures for 2 h. (a) 400 °C, (b) 800 °C, (c) 900 °C, and (d) 1100 °C (rate 5 K min^{-1}).

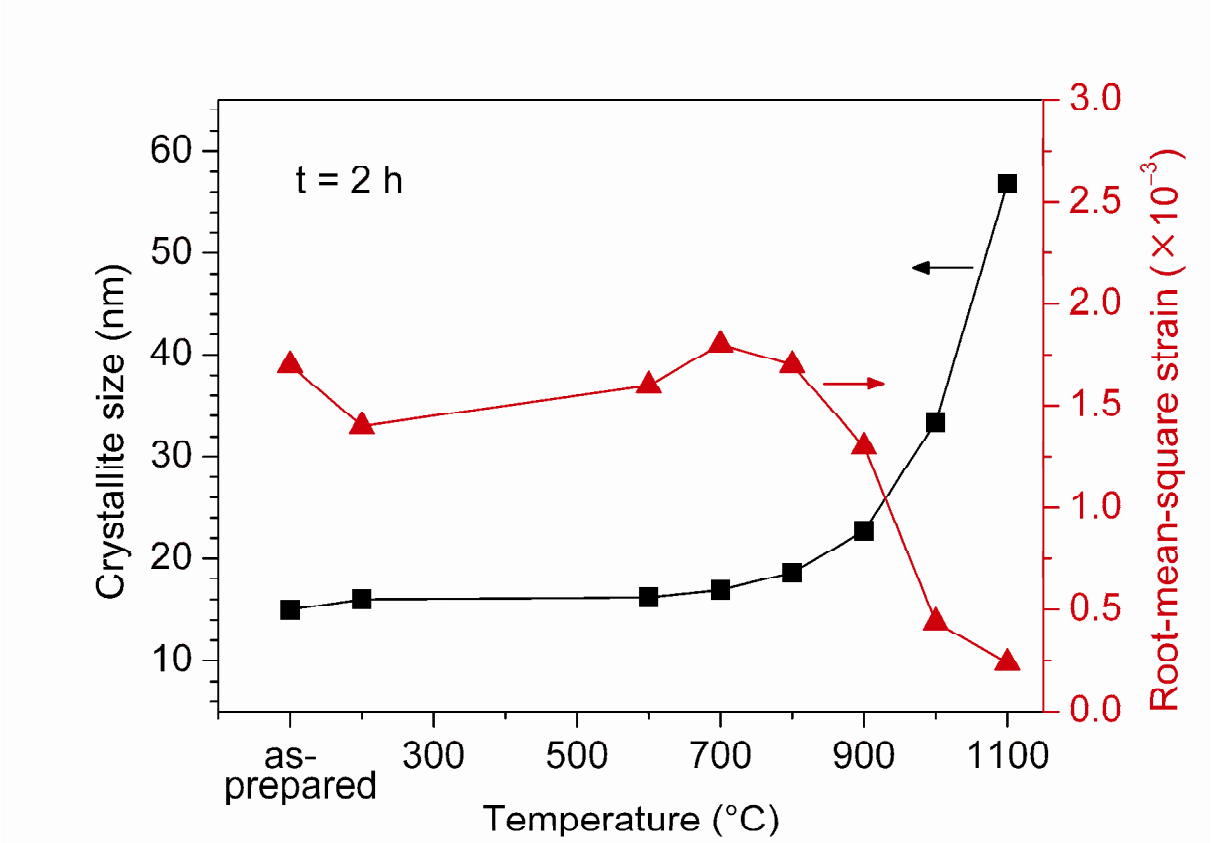

Fig. 4 Evolution of the volume-weighted average crystallite size and the root-mean-square strain versus heating temperature of BFN-8M powders.

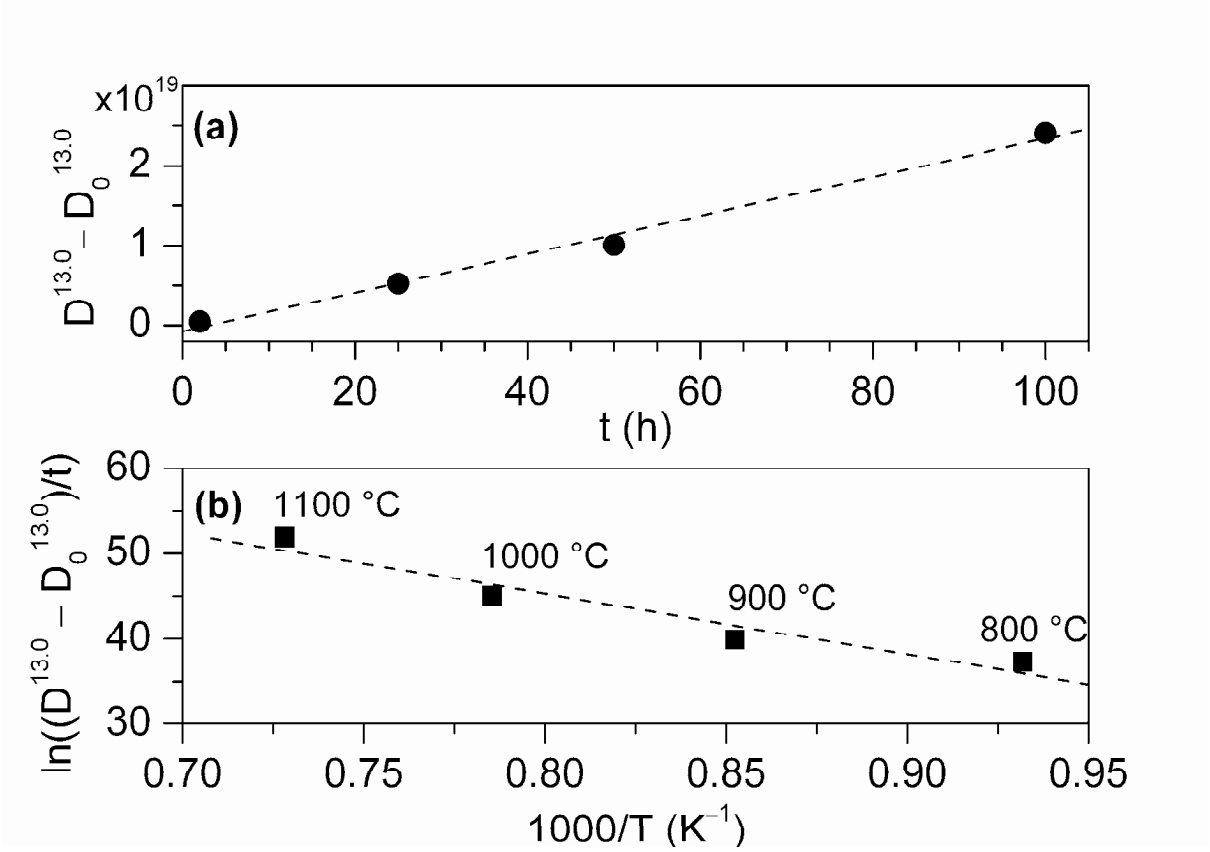

Fig. 5 (a) Plot of $D^{13.0}–D_0^{13.0}$ (crystallite size) versus t (annealing time) for sample BFN-8M heated at 900 °C. (b) Plot of $\ln((D^{13.0}–D_0^{13.0})/t)$ as a function of T^{-1} at a annealing time of 2 h (heating rate 5 K min^{-1}).

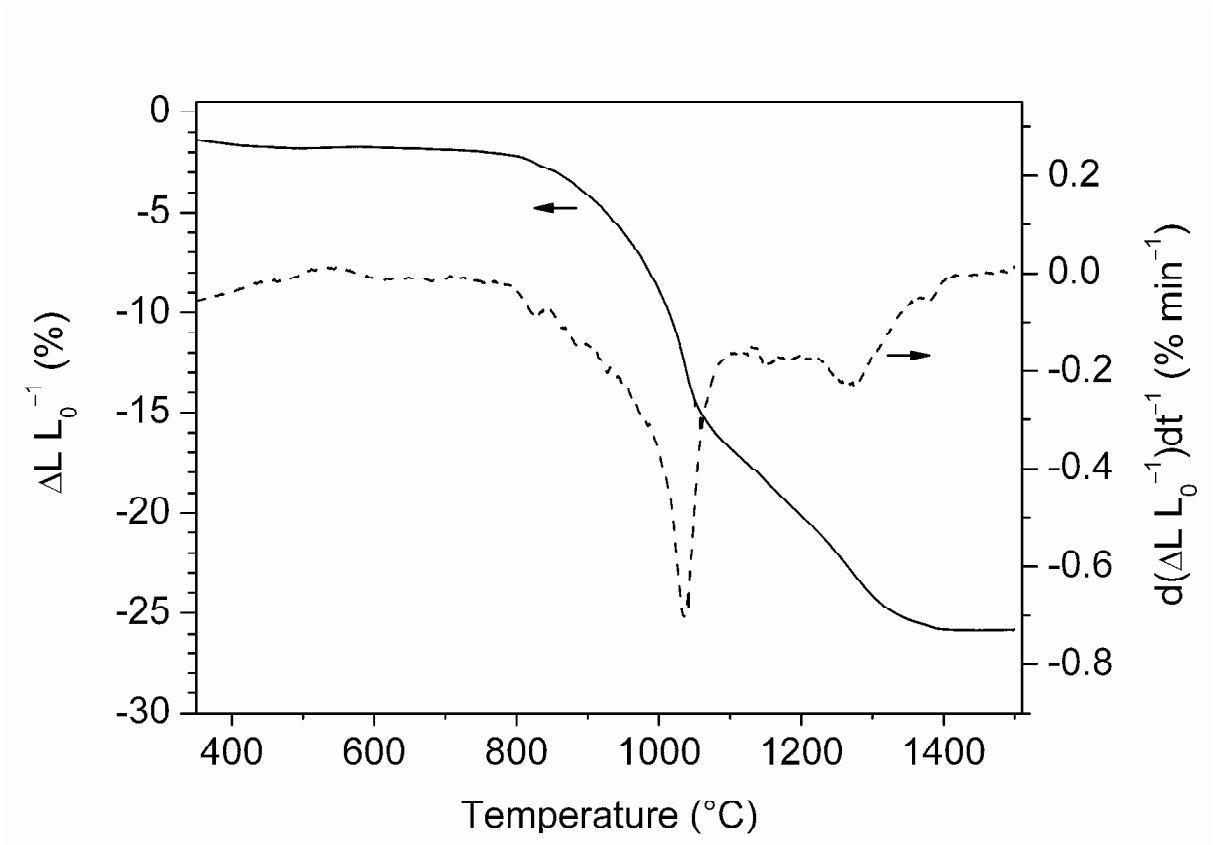

Fig. 6 Non-isothermal dilatometric measurement in flowing air up to 1500 °C (heating rate 5 K min^{-1}) of a green body of BFN-8M.

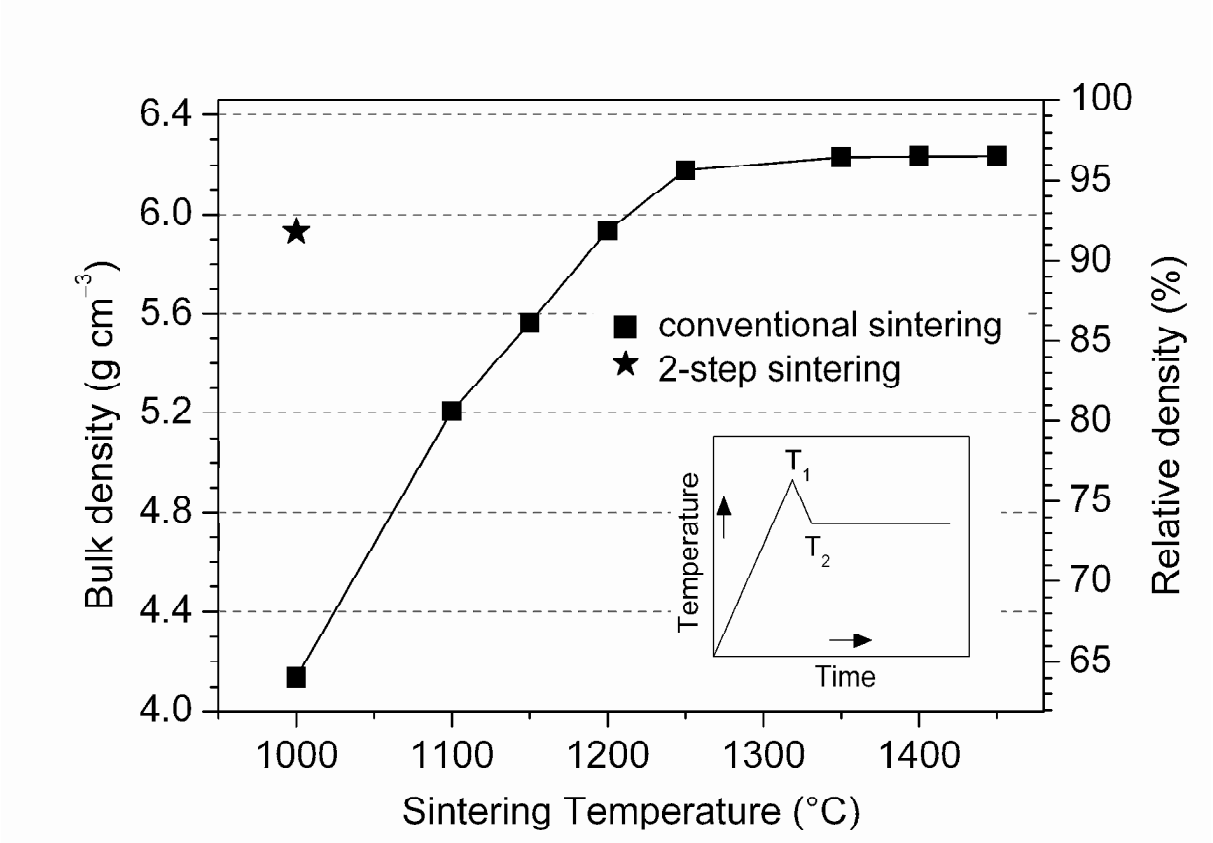

Fig. 7 Final bulk densities versus sintering temperature of ceramic bodies from powder BFN-8M after a soaking time of 1 h (conventional sintering) and 10 h (two-step sintering). The inset schematically shows the two-step sintering process.

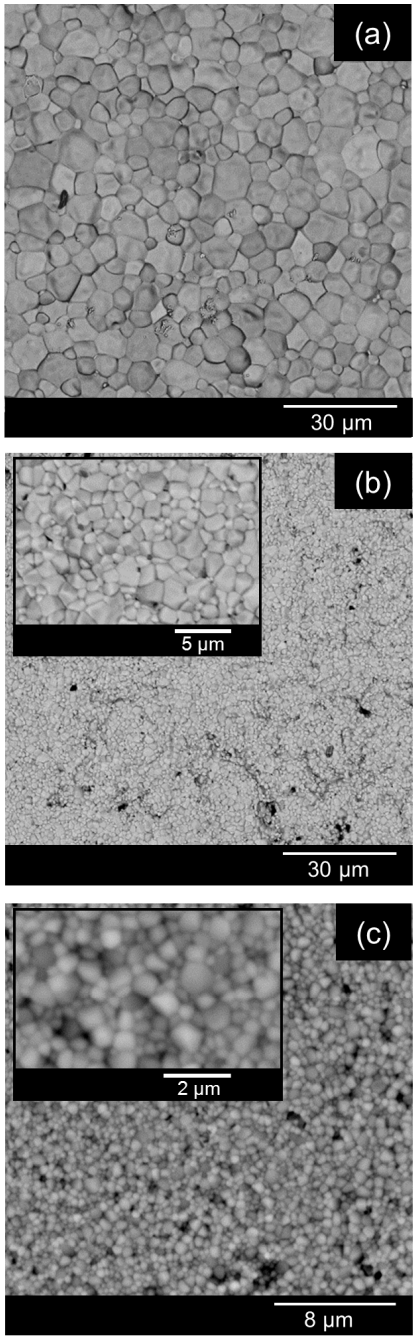

Fig. 8 SEM surface images (BSE mode) of ceramic bodies of BFN-8M. (a) conventional sintering at 1350 °C, 1 h; (b) conventional sintering at 1250 °C, 1 h; (d) two-step sintering at T_2 = 1000 °C, 10 h.

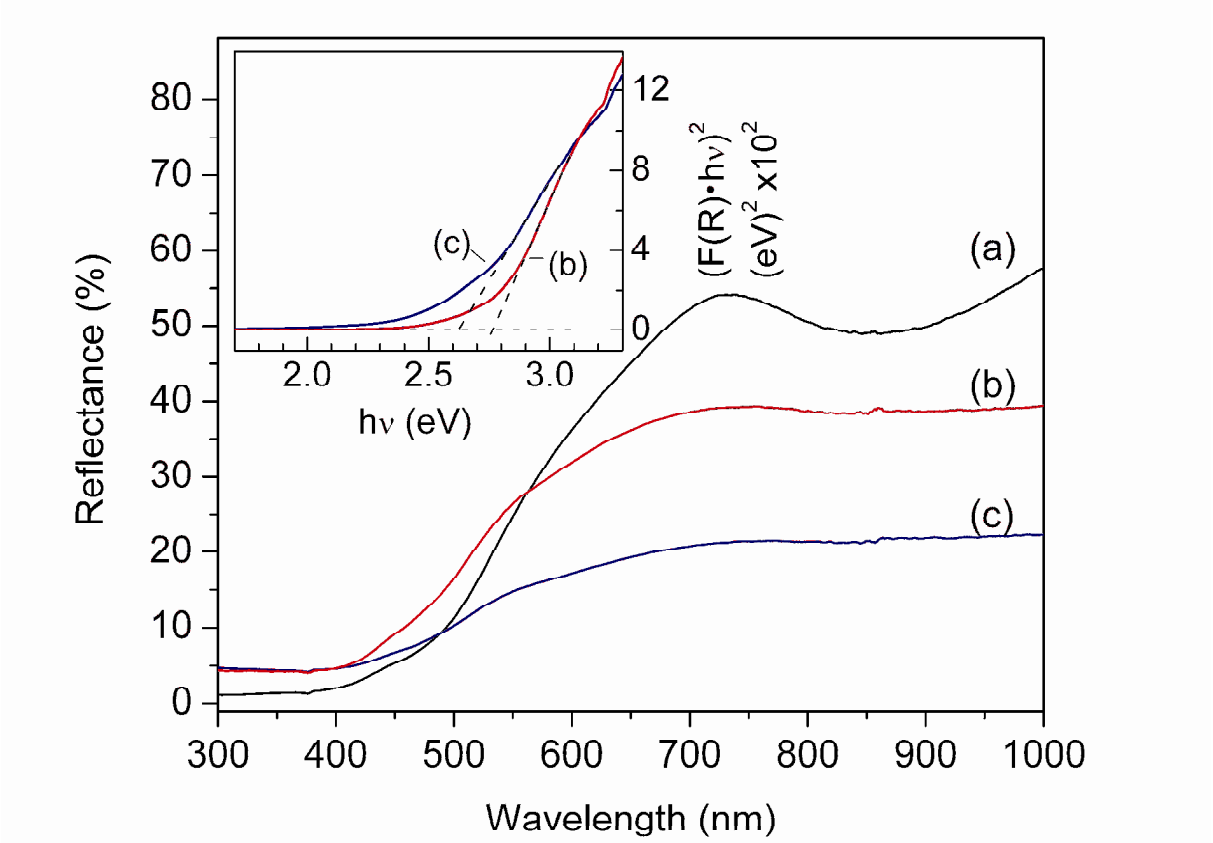

Fig. 9 Diffuse reflectance spectra of BFN-8M samples. (a) as-prepared, (b) after conventional sintering at 1000 °C for 1 h, and (c) 1200 °C for 1 h. The inset shows plots of $(F(R)\cdot h\nu)^2$ versus hν of samples sintered at (a) 1000 °C and (b) 1200 °C for 1 h.

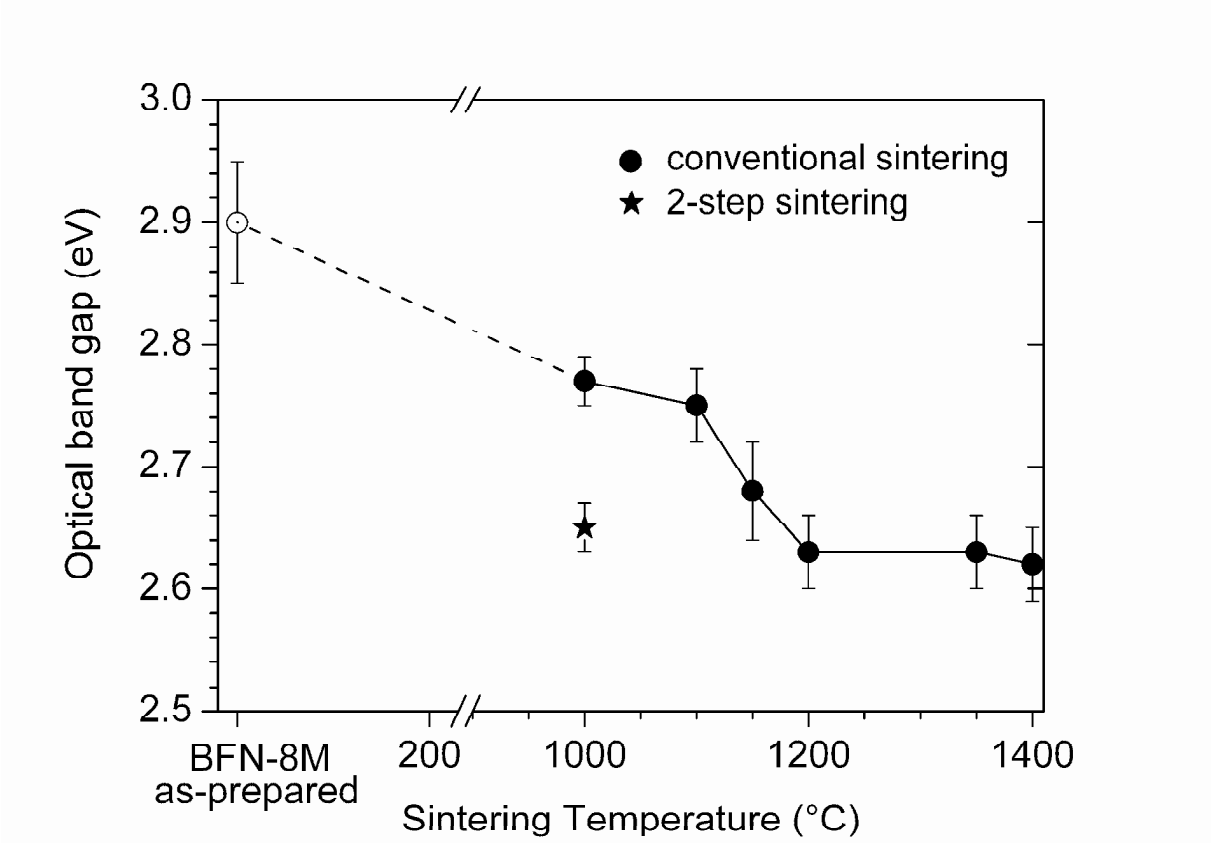

Fig. 10 Optical band gap versus sintering temperature of conventionally sintered (soaking time 1 h) and two-step sintered ceramics of BFN-8M.

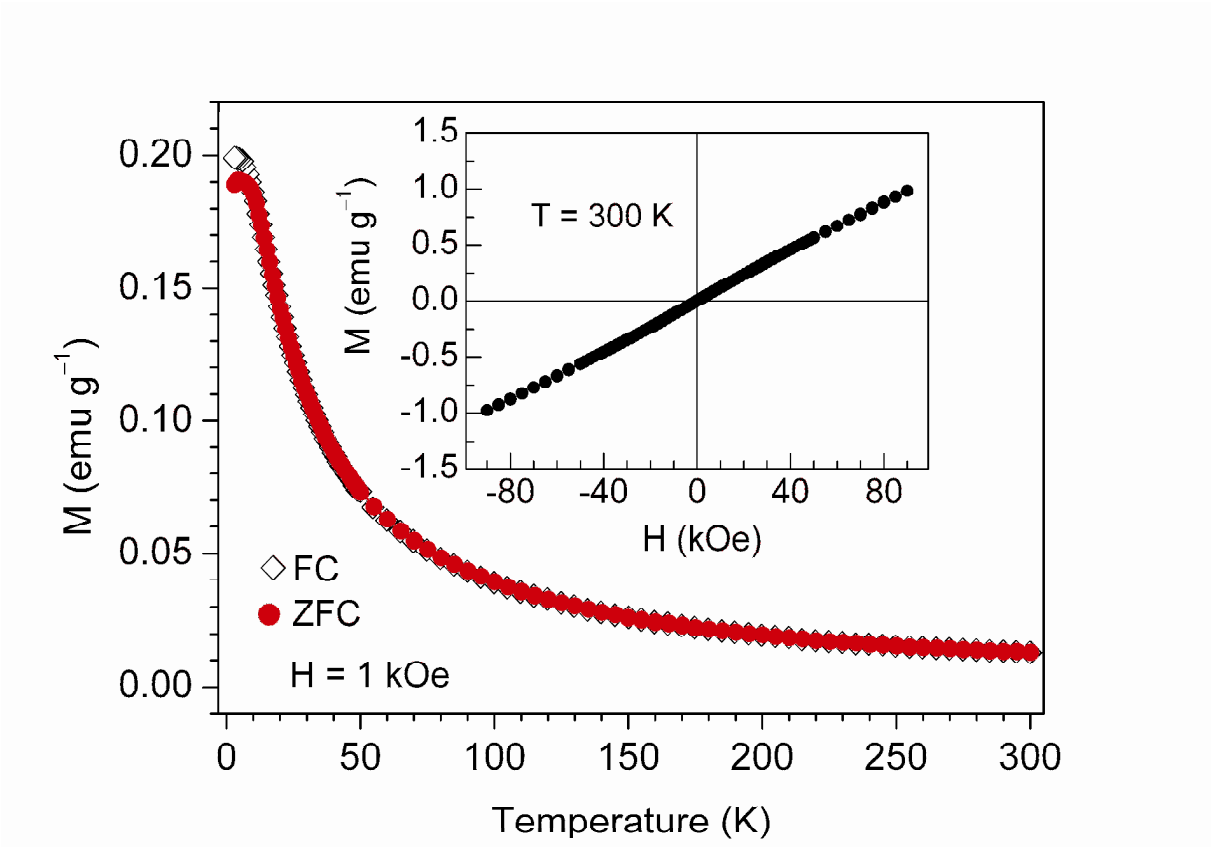

Fig. 11 Temperature dependence of the magnetization under zero-field cooled (ZFC) and field cooled (FC) conditions for the as-prepared powder BFN-8M. The inset shows the magnetization versus applied field at 300 K.

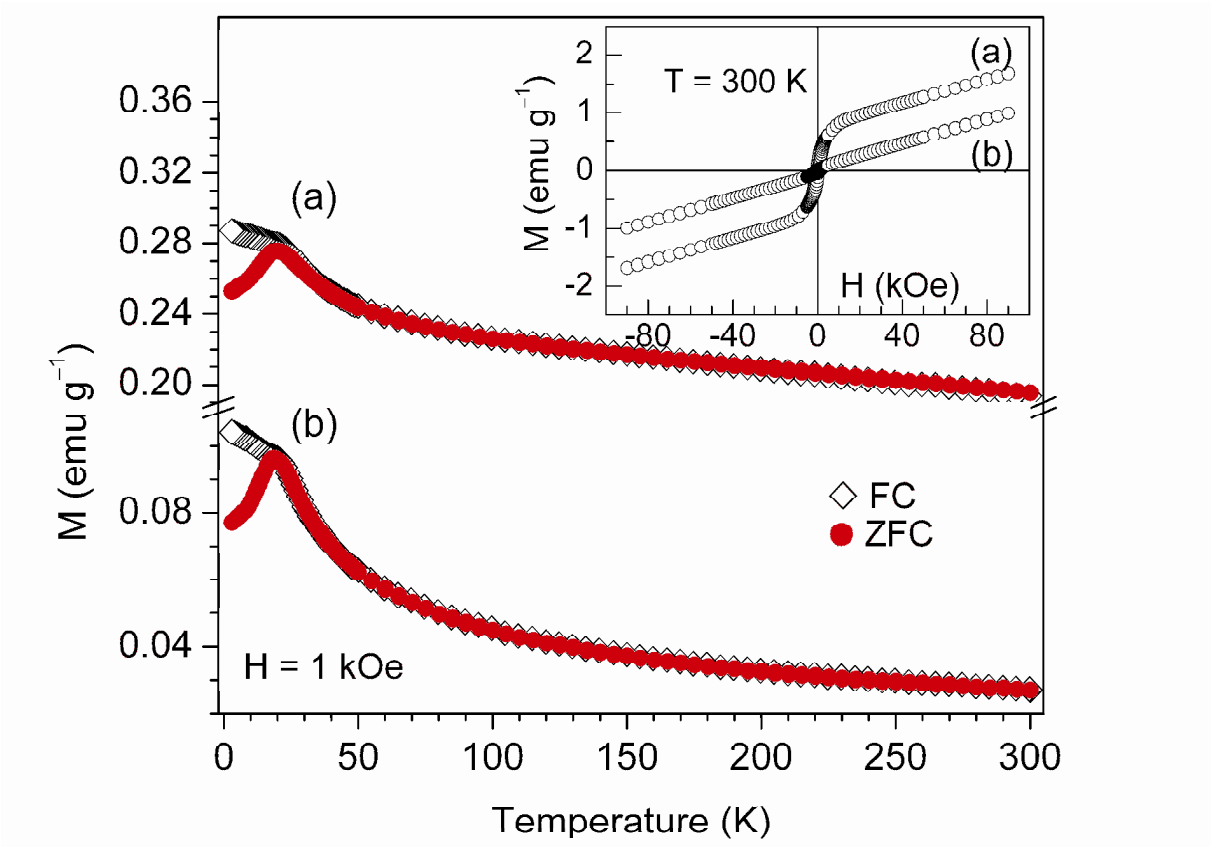

Fig. 12 Temperature dependence of the magnetization under zero-field cooled (ZFC) and field cooled (FC) conditions for ceramic bodies. (a) sintered at 1350 °C for 1 h, and (b) sintered at 1350 °C for 50 h. The inset shows the magnetization versus applied field at 300 K.

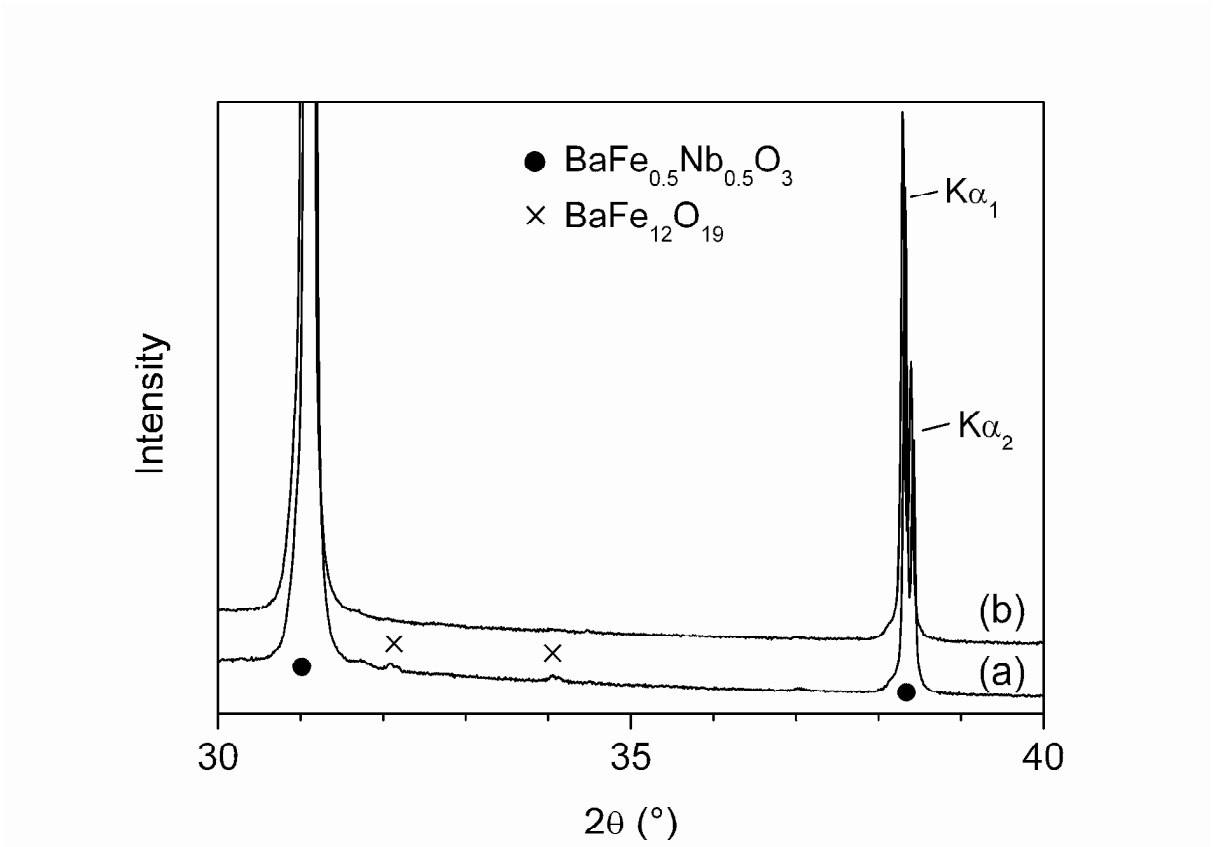

Fig. 13 XRD patterns of ceramic bodies conventionally sintered at 1350 °C for (a) 1 h and (b) 50 h. The patterns were recorded with a counting time of 10 s per data point.

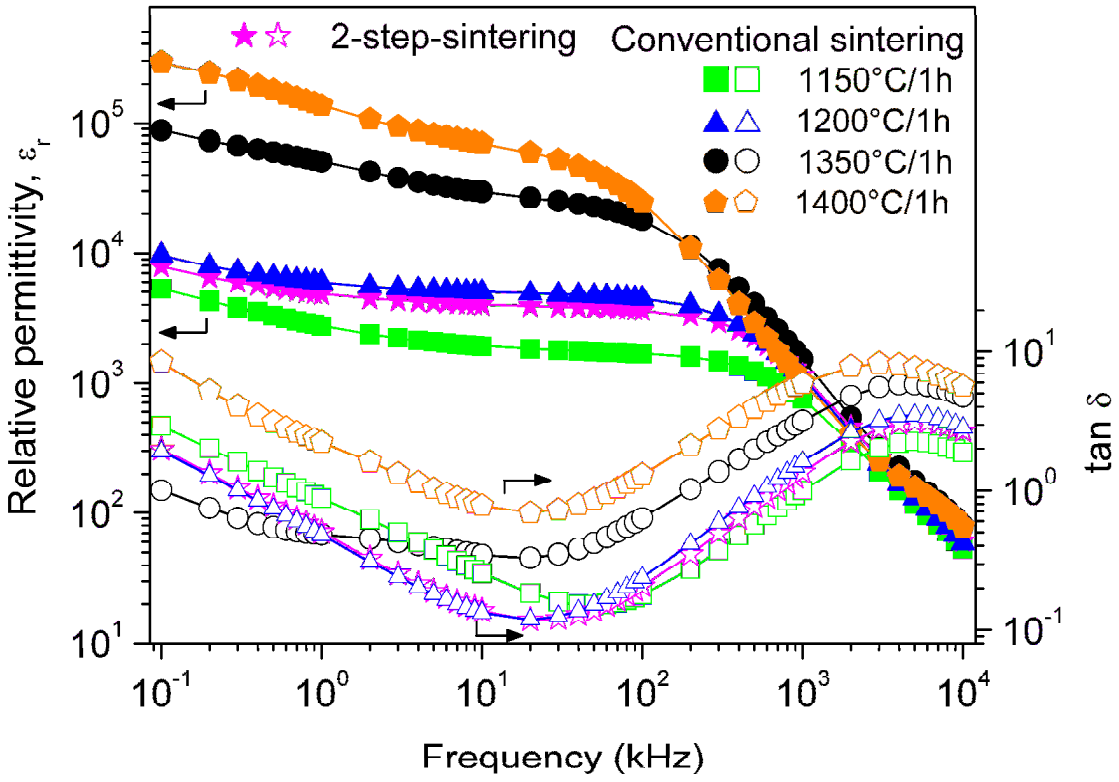

Fig. 14 Frequency dependence of the real part of the relative permittivity (ε_r) and the dissipation factor (tan δ) at room temperature (22 °C) for BFN-8M ceramic bodies obtained from the indicated sintering regimes.

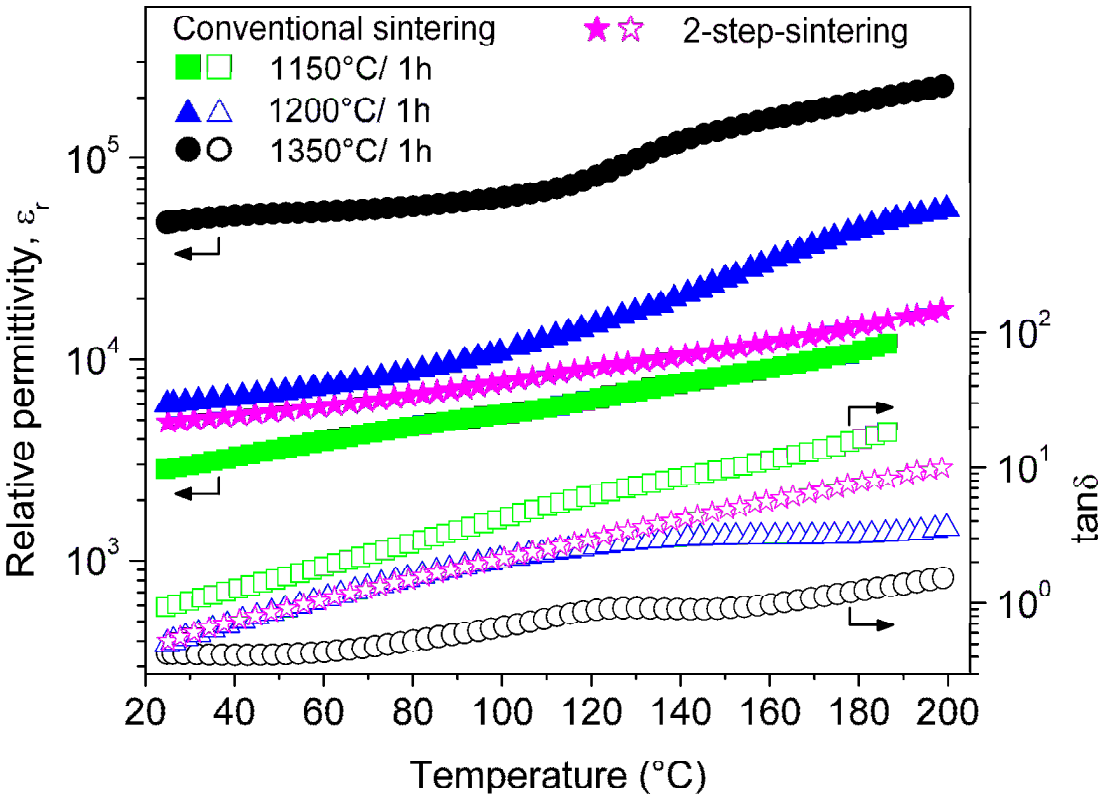

Fig. 15 Temperature dependence of ε_r and tan δ at 1 kHz for BFN-8M ceramic bodies obtained from the indicated sintering regimes.

Supporting Information

Investigations of $BaFe_{0.5}Nb_{0.5}O_3$ nano powders prepared by a low temperature aqueous synthesis and resulting ceramics

Roberto Köferstein* and Stefan G. Ebbinghaus

Institute of Chemistry, Martin Luther University Halle-Wittenberg, Kurt-Mothes-Strasse 2, 06120 Halle, Germany.

* Corresponding author. Tel.: +49-345-5525630; Fax: +49-345-5527028.
E-mail address: roberto.koeferstein@chemie.uni-halle.de

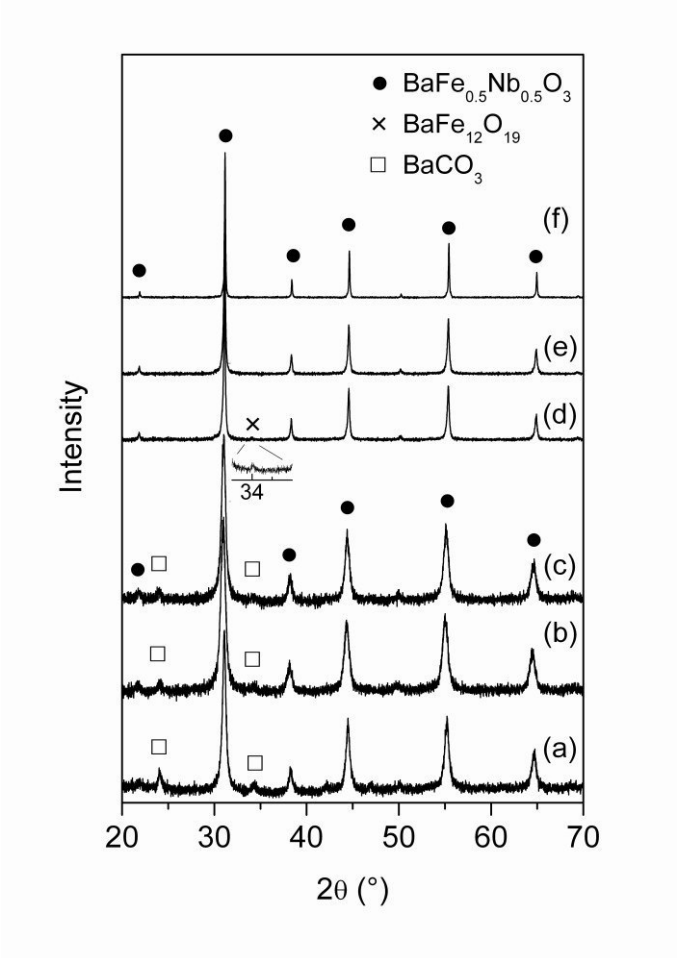

Fig. S1: XRD patterns of as-prepared powders. (a) BFN-6M, (b) BFN-8M, (c) BFN-14M, and samples heated at 1000 °C for 2 h (rate 5 K min^{-1}) of (d) BFN-6M, (e) BFN-8M, (f) BFN-14M.